Measurement error analysis of surface-bonded distributed fiber-optic strain sensor subjected to linear gradient strain: Theory and experimental validation

Xing Zheng[1], Bin Shi[1,*], Cheng-Cheng Zhang[1,2,3,*], Lei Zhang[1,4], Yijie Sun[5], and Heming Han[1]

[1] School of Earth Sciences and Engineering, Nanjing University, Nanjing, Jiangsu 210023, China
[2] Yuxiu Postdoctoral Institute, Nanjing University, Nanjing, Jiangsu 210023, China
[3] Nanjing University High-Tech Institute at Suzhou, Suzhou, Jiangsu 215123, China
[4] State Key Laboratory of Hydroscience and Engineering, Tsinghua University, Beijing 100084, China
[5] College of Transportation Science and Engineering, Nanjing Tech University, Nanjing, Jiangsu 210009, China

[*] Correspondence to: shibin@nju.edu.cn (B.S.), zhang@nju.edu.cn (C.-C.Z.)

Abstract: Strain transfer analysis is an important means of correcting the measurement error of embedded or surface-bonded distributed fiber-optic sensors, but the effect of host strain patterns has not been well elucidated. Here, a theoretical model for strain transfer analysis of surface-bonded multi-layered fiber-optic sensor subjected to a linear gradient strain was established. Closed-form solutions were obtained for both single- and bi-linear strain distributions, and, in particular, a simple method was described for determining the strain transfer coefficient at the turning point of a bi-linear type strain. The presented model was validated through laboratory testing with high-spatial resolution strain profiles acquired by optical frequency-domain reflectometry. Furthermore, parametric analyses were performed to investigate the influences of mechanical and geometrical properties of protective and adhesive layers on the strain transfer performance, shading light on the design, installation, and measurement error correction of fiber-optic sensors after accounting for the effect of host strain distribution.

Keywords: distributed fiber-optic sensor, measurement error, surface-bonding, strain transfer, optical frequency-domain reflectometry

1. Introduction

Distributed fiber-optic (FO) sensors have been widely used in structural health monitoring (SHM) because of their unique advantages such as distributed and long-distance measurement, high precision, anti-interference, and easy installation [1–12]. The common sensing optical fiber is only hairline thick and fragile, which usually needs a multi-layered sheath package to form an FO cable or sensor to resist the harsh engineering environment [13–15]. However, the strain loss will occur during the process of strain transfer from the monitored structure to the fiber core, which will result in the strain measurement error of a distributed FO sensing system [16–18]. Therefore, it is very important to understand the host-to-core strain transfer mechanism for the evaluation and correction of FO strain measurement error.

The strain transfer theory of FO sensors has attracted a great deal of attention from researchers and practitioners. To date, most research achievements on this aspect are based on the shear lag theory of composite materials introduced by Cox [19]. The early research began with embedded FO sensors in engineering materials [20]. For example, Nani et al. determined the strain transfer coefficient between FO sensor and concrete structure and found that the strain transfer coefficient is higher when the Young's modulus of the protective layer is close to that of the fiber core [21]. In 1998, Ansari and Yuan established a strain transfer model of an embedded fiber Bragg grating (FBG) sensor subjected to uniform strain using the shear lag theory, which provides an important reference case for later theoretical analysis and engineering practice [16]. Li et al. improved the model in [16] based on the assumption that the strain gradient at the midpoint of each layer of FO sensor is approximately equal; the derived result was closer to the actual situation [17]. On this basis, the strain transfer mechanism of FBG sensors under non-axial uniform strain was studied [22]. By introducing Goodman's hypothesis, Wang et al. further considered the properties of host materials around the fiber and analyzed the influence of host viscoelasticity and environment temperature on the strain transfer coefficient, which enriched the research on the strain transfer mechanism of embedded FO sensors [23].

Different from that of embedded FO sensors, strain transfer analysis of surface-bonded FO sensors should take into extra consideration the influence of geometric and physical properties of the adhesive layer [24]. Wan et al. introduced an axisymmetric model of surface-bonded FBG sensor to study the influence of adhesive layer width and bottom thickness on the strain transfer coefficient, and the reliability of the model was further validated through experiments and finite element analysis [25]. Considering the possible gap between FO cable and adhesive layer, Her et al. proposed an elaborate analytical model for strain transfer analysis of surface-bonded FO sensors [26,27]. Xin et al. derived the strain transfer model in the polar coordinate system and discussed the strain transfer phenomenon observed in crack detection [28]. Recently, thanks to the development of the high-performance distributed FO sensing technology—optical frequency-domain reflectometry (OFDR), Zhang et al. systematically investigated the effect of mechanical parameters and bonding method of FO cable on the strain transfer efficiency from both theoretical and experimental sights [29]. Falceteli et al. developed a strain transfer model of multi-layered FO cable and derived the distribution of strain transfer coefficient for a non-zero boundary condition; the theoretical analyses were more consistent with actual observations [30].

From the above cases, it can be found that the strain transfer theory is primarily developed for FBG sensors, and most studies have adopted the assumption that the strain distribution of host material is uniform. However, in actual SHM applications,

the structural strain is often a complex and non-uniform strain. To this aim, a strain transfer model of the surface-bonded FO sensor with a multi-layered structure subjected to a linear gradient strain was established. Analytical solutions for both single- and multi-linear type strain distributions were derived. The proposed model was validated by laboratory experiments with high-resolution strain profiles recorded using an OFDR interrogator. This study may provide a theoretical basis for the error analysis and correction of the surface-bonded distributed FO sensor subjected to a linear gradient strain, and guide the design and installation of distributed FO sensors for SHM purposes.

2. Theoretical model

2.1. Model formulation

A distributed FO sensing system usually employs a packaged single-mode optical fiber (FO cable) as the sensing element and transmission medium. The deformation or temperature of the structure can be monitored by bonding the sensor on the structure surface or directly embedding it into the structure. Extending the research of Falcetelli et al. [30], a strain transfer model of surface-bonded distributed FO sensor with an *n*-layered structure subjected to a non-uniform host strain is established (Fig. 1). The proposed model is based on the following assumptions:

(1) Both the core and cladding of the sensor are silica, which can be regarded collectively as a single layer named fiber core.

(2) The fiber core, each protective layer, and the adhesive layer are all linear elastic materials; the bonding between different layers is good and there is no relative slip.

(3) Only the shear stress transfer process of each protective layer and adhesive layer within the bonding range of FO sensor is considered.

The analytical model is established in the polar coordinate system where x represents the position along the axis of the sensor, r represents the radial position, and α represents the angle. Referring to Fig. 1(b), the mechanical equilibrium of the fiber core element can be expressed as follows:

$$(\sigma_c + \mathrm{d}\sigma_c)\pi r_c^2 - \sigma_c \pi r_c^2 + \int_0^{2\pi} \tau(x, r_c) r_c \mathrm{d}\theta \cdot \mathrm{d}x = 0 \tag{1}$$

where r_c is the outside radius of the fiber core layer, σ_c donates the normal stress on the cross section of the fiber core, and $\tau(x, r_c)$ donates the shear stress on the interface between the fiber core and the first protective layer.

Eq. (1) can be reduced to the following:

$$\tau(x, r_c) = -\frac{r_c}{2} \frac{\mathrm{d}\sigma_c}{\mathrm{d}x} \tag{2}$$

According to assumption (3), the force equilibrium of the first protective layer can be expressed as follows:

$$\int_{\alpha}^{\pi-\alpha} \tau(x, r) r \mathrm{d}\theta \cdot \mathrm{d}x - \int_0^{2\pi} \tau(x, r_c) r \mathrm{d}\theta \cdot \mathrm{d}x = 0 \tag{3}$$

where α is the angle between the boundary point of the adhesive layer and the horizontal line, and $\tau(x, r)$ donates the shear stress on the interface between the first and second protective layers. By combining Eqs. (2) and (3), $\tau(x, r)$ can be obtained as follows:

$$\tau(x, r) = -\frac{\pi}{\pi - 2\alpha} \frac{r_c^2}{r} \frac{\mathrm{d}\sigma_c}{\mathrm{d}x} \tag{4}$$

Based on assumption (2), the fiber core and each protective layer are all linear elastic materials. Employing Hooker's law, the shear strain at the interface between the

first and second protective layers can be expressed as follows:

$$\gamma(x,r) = -\frac{1}{G_1}\frac{\pi}{\pi-2\alpha}\frac{r_c^2}{r}E_c\frac{\mathrm{d}\varepsilon_c}{\mathrm{d}x} \tag{5}$$

where $\gamma(x,r)$ donates the shear strain at the interface between the first and second protective layers, G_1 donates the shear modulus of the first protective layer, E_c donates the Young's modulus of the fiber core, and ε_c donates the strain of the fiber core. Because the radial displacement is far less than the axial displacement, Eq. (5) can be converted to:

$$\gamma(x,r) \cong \frac{\partial u}{\partial r} = -\frac{1}{G_1}\frac{\pi}{\pi-2\alpha}\frac{r_c^2}{r}E_c\frac{\mathrm{d}\varepsilon_c}{\mathrm{d}x} \tag{6}$$

where u donates the axial displacement. The axial displacement on the boundary of the first protective layer can be obtained by integrating Eq. (6):

$$\int_{r_c}^{r_1}\frac{\partial u}{\partial r} = \int_{r_c}^{r_1} -\frac{1}{G_1}\frac{\pi}{\pi-2\alpha}\frac{r_c^2}{r}E_c\frac{\mathrm{d}\varepsilon_c}{\mathrm{d}x}\mathrm{d}r \tag{7}$$

$$u_1 - u_c = -\frac{1}{G_1}\frac{\pi}{\pi-2\alpha}r_c^2E_c\frac{\mathrm{d}\varepsilon_c}{\mathrm{d}x}\ln\frac{r_1}{r_c} \tag{8}$$

where u_1 and u_c donate the axial displacement at the outside boundary of the fiber core and the first protective layer, respectively.

The same derivation is made for the other protective layers and the adhesive layer, and the following result can be obtained:

$$u_h - u_c = -\frac{\pi}{\pi-2\alpha}r_c^2E_c\frac{\mathrm{d}\varepsilon_c}{\mathrm{d}x}\left[\frac{1}{G_\mathrm{a}}\ln\frac{r_\mathrm{a}}{r_\mathrm{n}} + \frac{1}{G_n}\ln\frac{r_\mathrm{n}}{r_{\mathrm{n}-1}} + \cdots + \frac{1}{G_2}\ln\frac{r_2}{r_1} + \frac{1}{G_1}\ln\frac{r_1}{r_c}\right] \tag{9}$$

where u_h represents the axial displacement on the interface between the adhesive layer and the host; r_n and G_n represent the radius and shear modulus of the nth protective layer, respectively; G_a donates the shear modulus of the adhesive layer; and r_a donates the equivalent radius of the rubber layer, which can be calculated from Eq. (10) according to the geometric characteristics of the model (Fig. 1(a)):

$$r_\mathrm{a} = \frac{1}{\pi-2\alpha}\int_{\alpha}^{\pi-\alpha}\left[r_\mathrm{n}(1-\sin\alpha)+t\right]\mathrm{d}\theta = r_\mathrm{n} + t - \frac{2r_\mathrm{n}\cos\alpha}{\pi-2\alpha} \tag{10}$$

where t represents the thickness of the adhesive layer from the sensor bottom to the host surface (see Fig. 1(a)). Here, a shear lag coefficient k is introduced, then Eq. (9) can be simplified as follows:

$$u_h - u_c = -\frac{1}{k^2}\frac{\mathrm{d}\varepsilon_c}{\mathrm{d}x} \tag{11}$$

where the shear lag coefficient k can be expressed as follows:

$$k = \sqrt{\frac{\pi-2\alpha}{\pi r_c^2E_c\left[\frac{1}{G_\mathrm{a}}\ln\frac{r_\mathrm{a}}{r_\mathrm{n}} + \frac{1}{G_\mathrm{n}}\ln\frac{r_\mathrm{n}}{r_{\mathrm{n}-1}} + \cdots\frac{1}{G_2}\ln\frac{r_2}{r_1} + \frac{1}{G_1}\ln\frac{r_1}{r_c}\right]}} \tag{12}$$

Since the first derivative of axial displacement with respect to x is the axial strain, Eq. (11) can be converted to:

$$\frac{\mathrm{d}^2\varepsilon_c}{\mathrm{d}x^2} - k^2\varepsilon_c = -k^2\varepsilon_h(x) \tag{13}$$

where $\varepsilon_h(x)$ represents the strain distribution of the host material. The solution of Eq. (13) is obtained by solving the second order linear nonhomogeneous differential equation with constant coefficients:

$$\varepsilon_c(x) = C_1 e^{-kx} + C_2 e^{kx} + \varepsilon_h(x) \tag{14}$$

where C_1 and C_2 donate the integration constants which can be determined according to boundary conditions. The strain transfer coefficient of the surface-bonded FO sensor can be defined as the ratio of the fiber core strain to the host strain:

$$z(x) = \frac{\varepsilon_c}{\varepsilon_h} \tag{15}$$

2.2. Analytical solutions

2.2.1. Single linear gradient strain

When a cantilever beam with a uniform cross section is subjected to a point load at the free end, the strain distribution of the beam will be a single linear gradient. Consider such a strain distribution as shown in Fig. 2, the corresponding strain transfer coefficient for the boundary condition $z(\pm L) = 0$ can be derived as:

$$z(x) = 1 - \frac{1}{ax + b}\left[\frac{aL \cdot \sinh(kx)}{\sinh(kL)} + \frac{b \cdot \cosh(kx)}{\cosh(kL)}\right] \tag{16}$$

The influences of the bonding length $2L$ and the strain gradient a on the strain transfer coefficient are studied through a simple example. In this example, the shear lag coefficient k is 6. Fig. 3 shows that the curves of strain transfer coefficient of FO sensor subjected to a single linear gradient strain is similar to those under a uniform strain—there are obvious low strain sensing sections at both ends of the sensor, which is defined as the sensor section with strain transfer coefficients being lower than 0.95 (denoted by L_{low}). When the bonding length is long enough (>2 L_{low}), the strain transfer performance of the middle part of the cable is good. Therefore, in practical applications, the bonding length of the sensor should be longer than 2 L_{low}. By contrast, when the shear lag coefficient k is small (corresponding to a poor strain transfer performance), the strain transfer coefficient will be affected by the host strain distribution, and the curve will incline to the side with a lower host strain. These results indicate that when the shear lag coefficient k is small due to the design or installation method of FO sensor, the influence of host strain distribution on the strain transfer coefficient should be considered to better evaluate and correct the measurement error.

2.2.2. Bilinear gradient strain

When a uniform beam is subjected to a three-point loading, its strain distribution will be a combination of two linear strain gradients as shown in Fig. 4. In this case, the analytical solution of the strain transfer coefficient can only be derived if the coefficient value at the turning point of the bilinear curve (e.g., $x = 0$ in Fig. 4) is predetermined in addition to the boundary conditions at the two sensor ends ($x = -L_1$, $x = L_2$). Assuming that the transfer coefficient is z_0 at the turning point, the analytical solution is derived as:

$$z(x)=\begin{cases}1+\dfrac{(z_0-1)\cdot b\cdot\sinh[k(L_1+x)]-(\mathrm{c}L_1-\mathrm{b})\sinh(kx)}{(\mathrm{a}x+\mathrm{b})\cdot\sinh(kL_1)} & -L_1\le x\le 0\\ 1+\dfrac{(z_0-1)\cdot b\cdot\sinh[k(L_2-x)]-(\mathrm{a}L_2+\mathrm{b})\sinh(kx)}{(\mathrm{a}x+\mathrm{b})\cdot\sinh(kL_2)} & 0<x\le L_2\end{cases} \tag{17}$$

Considering the continuity of fiber strain along the axial direction, if both sensor sections (L_1–0, 0–L_2) are long enough ($>L_{low}$), it is reasonable to assume that the strain transfer coefficient at the turning point is 1. By contrast, when the turning point is still within the low strain sensing section, the strain transfer coefficient at the turning point remains undetermined. In a numerical example we assume that the host strain distribution is as follows:

$$\varepsilon(x)=\begin{cases}1000x+1000 & -L_1\le x<0\\ -1000x+1000 & 0\le x\le L_2\end{cases} \tag{18}$$

Besides, we assume a strain transfer coefficient of 0.95 at the turning point to look at the strain transfer coefficient distribution along the sensor length (Fig. 5). It can be seen that the strain transfer coefficient profiles for single linear and bilinear gradient strains of host material are of the same pattern.

In actual applications, however, it is difficult to directly determine the strain transfer coefficient at the turning point. Here, a simple method is proposed to address this issue. First, the host strain along the whole sensor length (-L_1–L_2, Fig. 4) is assumed to have a gradient equivalent to that of the longer sensor section (0–L_2, Fig. 4). Then, a strain transfer coefficient distribution $z_e(x)$ is obtained according to the method described in section 2.2.1. Next, $z_e(x)\big|_{x=0}$ is taken as the approximate strain transfer coefficient z_0 at the turning point. Finally, the actual strain transfer coefficient profile is calculated using Eq. (17). The feasibility of this method will be verified through laboratory tests described in the following section.

3. Experimental validation

To validate the proposed strain transfer model, two laboratory tests were conducted where the host materials were subjected to multi-linear strains. In the first test, the cable bonding length was made sufficiently long and each cable section was longer than L_{low} to examine whether the transfer coefficient can be set to 1 at the turning point in the theoretical model. The second test was aimed at validating the analytical solution for a bilinear host strain distribution in case that the turning point is within the low strain sensing section.

3.1. Three-point bending test of aluminum alloy inclinometer tube

3.1.1. Test setup and procedure

A three-point bending test was conducted on a 4 m long aluminum alloy inclinometer tube installed with a 0.9 mm diameter tight-buffered FO strain sensing cable (Fig. 6). The test setup is shown in Fig. 7.

The FO cable was surface-bonded along the axial direction of the tube with epoxy resin. After the glue was cured, the inclinometer tube was symmetrically placed on the supports, and five dial gauges were installed at different positions above the pipe to record lateral displacements of the tube. The strain distributions of the cable were collected by an OSI-S OFDR interrogator with a spatial resolution of 1 mm and measurement accuracy of ±1 με. More details about the principle of OFDR can be

referred to [34–37]. The loading point was 2 m away from the left support and a 50 mm wide nylon belt was used for loading. The first loading applied was 16 kg with an increment of 25 kg, up to 141 kg in the sixth stage. After each loading stage was stable, the dial gauge and OFDR readings were respectively recorded to obtain the vertical displacement of the pipe and the strain profile of the cable.

3.1.2. Results and analyses

Fig. 8 shows the lateral displacement of the inclinometer tube recorded by the dial gauges under each load. According to the theory of elasticity, the theoretical strain distributions of the tube were calculated from the lateral displacement measurements. On the other hand, the distributions of strain transfer coefficient were calculated using Eq. (16) by assuming perfect strain transfers at the turning point and were then used to correct the OFDR-measured strains. The calculated values of L_{low} were no more than 0.11 m, far less the lengths between the supports to the load point (2 m and 1.82 m). The parameters of the FO cable and adhesive layer used in the theoretical analysis are listed in Table 1. These two strain profiles were compared (Fig. 9). The results show that except for the first loading stage, the corrected FO strains agreed well with the theoretical strains. It is noted that the strain curves had ~50 mm wide flat sections at the curve center due to the nylon belt used for loading. Despite this, there were no obvious low strain sensing sections at the turning point. Combined, this test validated the proposed analytical model and the assumption that the strain transfer coefficient at the turning point can be set to 1 when the bonded FO cable is long enough (greater than 2 L_{low}) while the turning point of host strain is outside the low sensing section. Moreover, these results highlight the advantage of distributed FO sensing in large-scale SHM campaigns.

3.2. Three-point bending test of PVC pipe

3.2.1. Test setup and procedure

To further verify the established theoretical model, an elaborate three-point bending test on a PVC pipe was carried out. A 3 m long PVC pipe with an outer diameter of 75 mm was used in the test. The G.652 double coating optical fiber manufactured by Corning Inc. was bonded on the surface of the pipe. The OFDR interrogator used for FO strain measurement was a Luna OBR 4413. The spatial resolution was 10 mm and the strain measurement accuracy was ±5 με.

The test setup is shown in Fig. 10. Two FO cables AB (orange) and ab (red) were bonded in parallel on the lower surface of the PVC pipe with epoxy resin. A redundant section was reserved at 0.1 m to the left of the loading point. The two ends of the PVC pipe were fixed by hinge supports. The pipe was deformed by hanging heavy objects in its middle part. The load from the first to the fourth stages was increased by 3 kg per stage, and the fifth and sixth stages were increased by 6 kg per stage.

3.2.2. Results and analyses

Strain distributions of the two FO cables obtained by the OFDR interrogator are shown in Fig. 11. The strain curves of cable AB exhibited symmetrical triangle distributions, and the position of the maximum strain point was consistent with the loading point. The strain curves of cable ab were divided into the bc section, redundant section, and ac section.

A comparison of strain values between sections BC and bc and that between sections AC and ac are shown collectively in Fig. 12. Although most strains of the two

cables were consistent, the deviations observed in the vicinity of point c were indicative of the existence of low strain sensing sections at the free end. According to the conclusions drawn in section 3.1 and considering that cable AB was sufficiently long, its strain values may be regarded as the true strains of the pipe. Therefore, the experimental strain transfer coefficients of section bc (or ac) can be determined by comparing its strain values to that of section BC (respectively, AC).

For the theoretical strain transfer coefficients of section bc, because the strain distribution of the pipe was the single linear gradient strain type (as indicated by the strain measurements of cable BC), they can be readily calculated using Eq. (16). A comparison between the experimental and theoretical strain transfer coefficients under the sixth loading stage (24 kg) is shown in Fig. 13. The parameters of the FO cable and adhesive layer used in the theoretical analysis were the same as those listed in Table 1 (note that the Corning fiber does not have a jacket). It can be seen from Fig. 13 that the two coefficient curves coincided with each other, hence validating the proposed theoretical model.

For the theoretical strain transfer coefficients of section ac, because the strain distribution of the pipe was the bilinear gradient strain type (as indicated by the strain measurements of cable AC), determining the strain transfer coefficient at the turning point (loading point) was a prerequisite. In this test, the length of the low strain sensing section (L_{low}) of the cable was about 0.11 m according to the experimental results of cable bc, which was longer than the distance between the loading point and point c (0.1 m). Therefore, the method proposed in section 2.2.2 was employed to determine the theoretical strain transfer coefficient distribution. The calculated z_0 was 0.954 and a comparison between the calculated and experimental strain transfer coefficient profile of cable ac under the sixth loading is shown in Fig. 14. Good agreement between the two curves illustrated the feasibility of the proposed method for evaluating the strain transfer performance of surface-bonded FO sensors subjected to a bilinear gradient strain.

4. Parametric study

To provide a reference for the design and installation of distributed FO strain sensors, the influences of the mechanical and geometric parameters of the protective layer and adhesive layer on the strain transfer efficiency were analyzed with the host strain distribution considered. The host strain profile was assumed to be a single linear gradient strain $\varepsilon(x) = 1000x + 1000$, and the bonding length of the FO sensor was 1 m. The strain transfer coefficients were calculated using Eq. (16). The parameters of the sensor and adhesive layer used in this parametric study were consistent with those used in section 3.2.2.

The influence of the shear modulus of the inner coating G_1 on the strain transfer coefficient is shown in Fig. 15. With the increase of G_1, the length of the low strain sensing section at both ends decreased, and the strain transfer performance of the sensor was greatly improved. Therefore, when designing FO strain sensing sensors, the coating materials with higher shear modulus should be selected to reduce the adverse effect of coating on the strain measurement performance of the sensor. Similarly, the effect of the shear modulus of the outer coating G_2 was investigated (Fig. 16). The higher the shear modulus of the outer coating, the better the strain transfer performance was. However, its influence was less evident compared to that of the inner coating. Specifically, the theoretical curves of G_2 = 50 and 5000 MPa almost overlapped, indicating that the protective layer especially the outer coating can protect the glass core with a limited impact on its strain transfer performance.

The effects of the shear modulus G_a and minimum thickness t of the adhesive layer were also examined. For G_a = 2.9, 29, and 290 MPa, the calculated shear lag coefficients k were 30.88, 31.79, and 31.88, respectively. Therefore, the strain transfer performance of the FO sensor will be slightly better with a larger adhesive shear modulus. The minimum thickness t was set to 20, 200, and 2000 μm; the calculated shear lag coefficients were 32.00, 31.79, and 31.47, respectively. The results indicated that a thicker adhesive layer will reduce the strain transfer performance but the impact is also limited. Considering that the adhesive can protect the surface-bonded FO sensor, the thickness of the adhesive layer can be increased appropriately to protect the sensor without significantly decreasing the sensor's sensing performance. Similarly, in the process of designing and producing strain sensing cables, the shear modulus of the protective layer can be larger and the thickness of the protective layer can be increased appropriately to improve the ability of the sensor to resist the harsh engineering environment while ensuring its strain transfer performance.

5. Conclusions

In this paper, a strain transfer model of the surface-bonded multi-layered distributed FO sensor subjected to a linear gradient strain was established. Two laboratory tests were conducted to validate the proposed model. Once the theoretical model was verified, a parametric study was performed to investigate the influences of host strain distribution and mechanical and geometric characteristics of both FO sensor and adhesive on the strain transfer performance of the sensor. The main findings of this study are the following:

- The influence of host strain distribution is mainly concentrated in the low strain sensing section at both ends of the bonding length. When the bonding length is short and the shear lag coefficient is low (corresponding to a large L_{low}), the effect of host strain pattern should be considered for measurement error correction.
- When the host material has a single linear gradient strain, the value of L_{low} at the lower strain end decreases with the increase of the gradient while that at the other end increases. The theoretical model proposed can well simulate the strain transfer performance of the FO sensor in this case.
- In case that the host material has a multi-linear gradient strain, if the cable bonding length is sufficiently long (each cable section is longer than L_{low}), the strain transfer coefficient of the turning point can be set to 1. If the turning point is in a low strain sensing section, the strain transfer coefficient of the turning point can be approximated by assuming that the host strain is of the single linear gradient type.
- The parametric analyses show that the strain transfer performance of the FO sensor can be significantly improved by employing coating materials with higher shear modulus. The effect of the protective layer on the strain transfer performance is limited, so the shear modulus and radius of the protective layer can be appropriately improved to enhance the sensor's ability to resist the harsh environment. During installation, to reduce the measurement error, the adhesive with higher shear modulus should be adopted, the bonding length should be long enough (>2 L_{low}), and the sensor should be close to the surface of the host material.

Acknowledgments

We thank Xing Wang and the staff of Suzhou Nanzee Sensing Technology Ltd. for their technical assistance. B.S. was supported by the National Natural Science Foundation of China (42030701). C.-C.Z. was supported by the Natural Science Foundation of Jiangsu Province (BK20200217), the National Key R&D Program of China (2019YFC1509601), and the Yuxiu Young Scholars Program of Nanjing University (2010619). L.Z. was supported by an open fund provided by the Hebei IoT Monitoring Engineering Technology Research Center (IOT202005).

References

[1] H.N. Li, D.S. Li, G.B. Song, Recent applications of fiber optic sensors to health monitoring in civil engineering. Engineering Structures, 2004, 26(11): 1647-1657.

[2] X.Y. Bao, L. Chen, Recent progress in distributed fiber optic sensors. Sensors, 2012, 12(7): 8601-8639.

[3] H.F. Pei, J. Teng, J.H Yin, R. Chen, A review of previous studies on the applications of optical fiber sensors in geotechnical health monitoring. Measurement, 2014. 58: 207-214.

[4] A. Barrias, J. Casas, S. Villalba, A review of distributed optical fiber sensors for civil engineering applications. Sensors, 2016. 16(5): 748.

[5] H. Mohamad, K. Soga, A. Pellew, P.J. Bennett, Performance monitoring of a secant-piled wall using distributed fiber optic strain sensing. Journal of Geotechnical and Geoenvironmental Engineering, 2011. 137(12): 1236-1243.

[6] H. Mohamad, K. Soga, P.J. Bennett, R.J. Mair, S.L. Chi, Monitoring twin tunnel interaction using distributed optical fiber strain measurements. Journal of Geotechnical and Geoenvironmental Engineering, 2012, 138(8):957-967.

[7] C.C. Zhang, H.H. Zhu, Q. Xu, B. Shi, G.X. Mei, Time-dependent pullout behavior of glass fiber reinforced polymer (GFRP) soil nail in sand. Canadian Geotechnical Journal, 2015, 52(6):671-681.

[8] Z.P. Song, D. Zhang, B. Shi, S.E. Chen, M.F. Shen, Integrated distributed fiber optic sensing technology-based structural monitoring of the pound lock. Structural Control and Health Monitoring, 2017, 24(7), e1954

[9] X. Wang, B. Shi, G.Q. Wei, S.E. Chen, H.H. Zhu, T. Wang, Monitoring the behavior of segment joints in a shield tunnel using distributed fiber optic sensors. Structural Control and Health Monitoring, 2018, 25(1): 2056.

[10] L. Pelecanos, K. Soga, M.Z.E.B. Elshafie, N.D. Battista, C. Kechavarzi, Y.G. Chang, Y. Ouyang, H.J. Seo, Distributed fiber optic sensing of axially loaded bored piles. Journal of Geotechnical and Geoenvironmental Engineering, 2018, 144(3):04017122.1-04017122.16.

[11] H. Wu, H.H. Zhu, C.C. Zhang, G.Y. Zhou, M. Azarafza, Strain integration-based soil shear displacement measurement using high-resolution strain sensing technology. Measurement, 2020, 166, 108210.

[12] P. Velha, T. Nannipieri, A. Signorini, et al., Monitoring large railways infrastructures using hybrid optical fibers sensor systems. IEEE Transactions on Intelligent Transportation Systems, 2020, 21(12):5177-5188

[13] C.Y. Hong, Y.F. Zhang, G.W. Li, M.X. Zhang, Z.X. Liu, Recent progress of using Brillouin distributed fiber sensors for geotechnical health monitoring. Sensors & Actuators A Physical 2017, 258:131-145.

[14] H.P. Wang, P. Xiang, L. Jiang, Strain transfer theory of industrialized optical fiber-based sensors in civil engineering: A review on measurement accuracy, design and calibration. Sensors and Actuators A: Physical, 2019, 285: 414-426.

[15] F. Bastianini, R.D. Sante, F. Falcetelli, D. Marini, G. Bolognini, Optical Fiber Sensing Cables for Brillouin-Based Distributed Measurements. Sensors, 2019, 19(23): 5172.

[16] F. Ansari, L.B. Yuan, Mechanics of Bond and Interface Shear Transfer in Optical Fiber Sensors. Journal of Engineering Mechanics, 1998, 124(4):385-394.

[17] D.S Li, Strain transferring analysis of fiber Bragg grating sensors. Optical Engineering, 2006, 45(2):409-411.

[18] C.C. Zhang, B. Shi, H.H. Zhu, B.J. Wang, G.Q. Wei, Toward distributed fiber‐optic sensing of subsurface deformation: A theoretical quantification of ground‐borehole‐cable interaction. Journal of Geophysical Research: Solid Earth, 2020, 125(3), e2019JB018878.

[19] H.L. Cox, The elasticity and strength of paper and other fibrous materials. British J of Applied Physics, 1951, 3(3):72.

[20] G. Duck, M. Leblanc, Arbitrary strain transfer from a host to an embedded fiber-optic sensor. Smart Materials and Structures, 2000. 9(4): 492-497.
[21] A. Nanni, C.C. Yang, K. Pan, J.S. Wang, R.R.M. Jr, Fiber-optic sensors for concrete strain/stress measurement. ACI Materials Journal, 1991, 88(3):257-264.
[22] H.N. Li, Strain transfer analysis of embedded fiber Bragg grating sensor under nonaxial stress. Optical Engineering, 2007, 46(5): p. 054402-054408.
[23] H.P. Wang, P. Xiang, Strain transfer analysis of optical fiber based sensors embedded in an asphalt pavement structure. Measurement Science and Technology, 2016, 27(7): 75106.
[24] G. Duck, G. Renaud, R. Measures, The mechanical load transfer into a distributed optical fiber sensor due to a linear strain gradient: embedded and surface bonded cases. Smart Materials and Structures, 1999, 8(2): 175-181.
[25] K.T. Wan, Quantitative sensitivity analysis of surface attached optical fiber strain sensor. IEEE Sensors Journal, 2014, 14(6): 1805-1812.
[26] S.C. Her, C.Y. Tsai, Strain measurement of fiber optic sensor surface bonding on host material. Transactions of Nonferrous Metals Society of China, 2009, 19(z1): 143-149.
[27] S.C. Her, C.Y. Huang, Effect of coating on the strain transfer of optical fiber sensors. Sensors, 2011. 11(7): 6926-6941.
[28] F. Xin, Z. Jing, C. Sun, X. Zhang, F. Ansari, Theoretical and experimental investigations into crack detection with BOTDR-distributed fiber optic sensors. Journal of Engineering Mechanics, 2013, 139(12): 1797-1807.
[29] Q. Zhang, Y. Sun, Z. Zhang, P. Zeng, F. Rong, Strain transfer in distributed fiber optic sensor with optical frequency domain reflectometry technology. Optical Engineering, 2019, 58(2).
[30] F. Falcetelli, L. Rossi, R.D.D. Sante, G. Bolognini, Strain transfer in surface-bonded optical fiber sensors. Sensors (Basel), 2020, 20(11).
[31] S.H. Kim, J.J. Lee, I.B. Kwon, FEM analysis of surface-mounted distributed optical fiber sensors. 2001: SPIE.
[32] S.M. Wei, J. Chai, Surface pasting methods and analyses of strain transfer in rock deformation tests using FBG. Chinese Journal of Geotechnical Engineering, 2011.33(4):578-592. (in Chinese)
[33] Z. Zhang, Y. Wang, Y. Sun, Q. Zhang, Z. You, X. Huang, Analysis and experimental study on the strain transfer mechanism of an embedded basalt fiber-encapsulated fiber Bragg grating sensor. Optical Engineering, 2017. 56(1):017105.
[34] J.H. Wu, H. Liu, P. Yang, B.J. Tang, G.Q. Wei, Quantitative strain measurement and crack opening estimate in concrete structures based on OFDR technology. Optical Fiber Technology, 2020, 60:102354.
[35] M. Froggatt, J. Moore, High-spatial-resolution distributed strain measurement in optical fiber with Rayleigh scatter. Applied Optics, 1998, 37(10):1735-40.
[36] S.T. Kreger, D.K. Gifford, M.E. Froggatt, B.J. Soller, M.S. Wolfe, High resolution distributed strain or temperature measurement in single-mode fiber using swept-wavelength interterometry, 18th International Conference Optical Fiber Sensing, 2006.
[37] H. Jean-Marie, M. Gautier, B. Sylvain, S. Jean, C. Jean-Robert, T. Frédéric, M. Erick, D. Jean-Philippe, B. Johan, B. Stéphane, Truly distributed optical fiber sensors for structural health monitoring: From the telecommunication optical fiber drawling tower to water leakage detection in dikes and concrete structure strain monitoring. Advances in Civil Engineering, 2010, 2010:13.

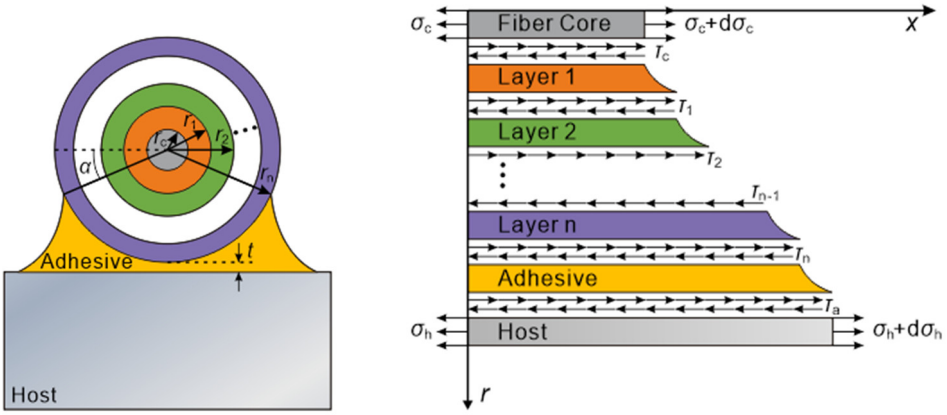

(a) (b)

Fig. 1. Strain transfer analysis of surface-bonded multi-layered FO sensor. (a) Cross section. (b) Stress states of multi-layers.

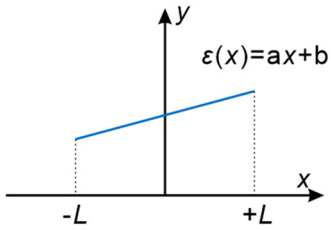

Fig. 2. Schematic diagram of a single linear gradient strain.

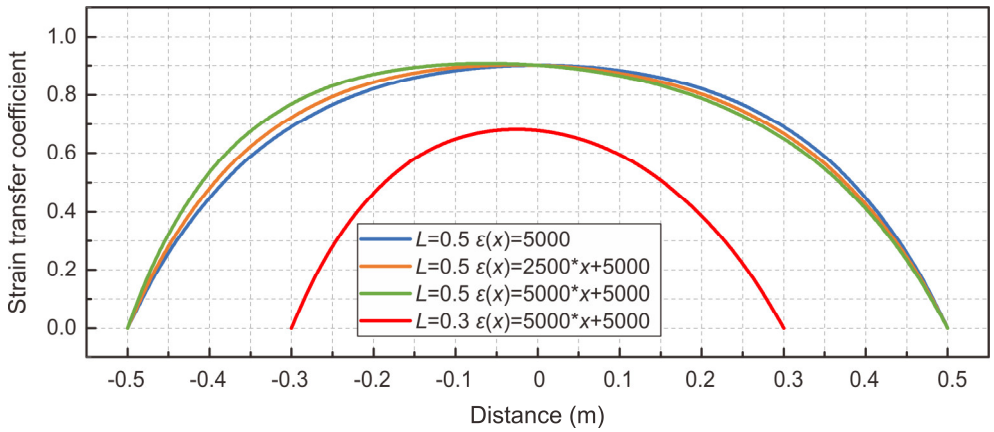

Fig. 3. Influence of bonding length and strain gradient on the strain transfer coefficient.

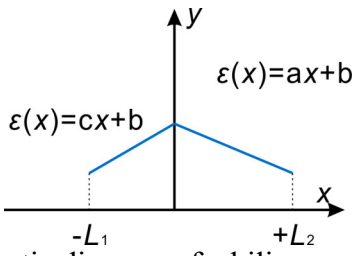

Fig. 4. Schematic diagram of a bilinear gradient strain.

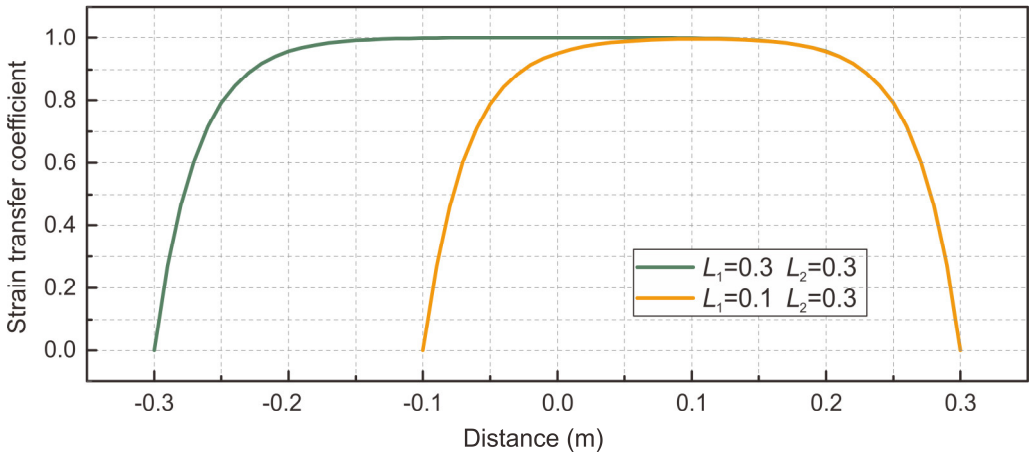

Fig. 5. Analytical results of strain transfer coefficient subjected to a bilinear host strain.

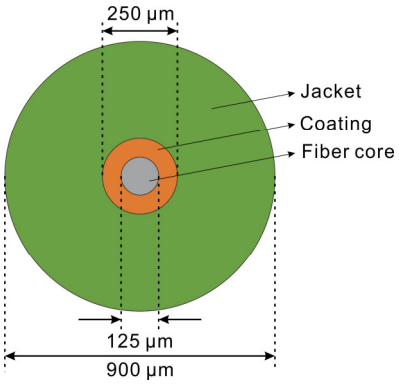

Fig. 6. Structure of 0.9 mm diameter tight-buffered FO strain sensing cable.

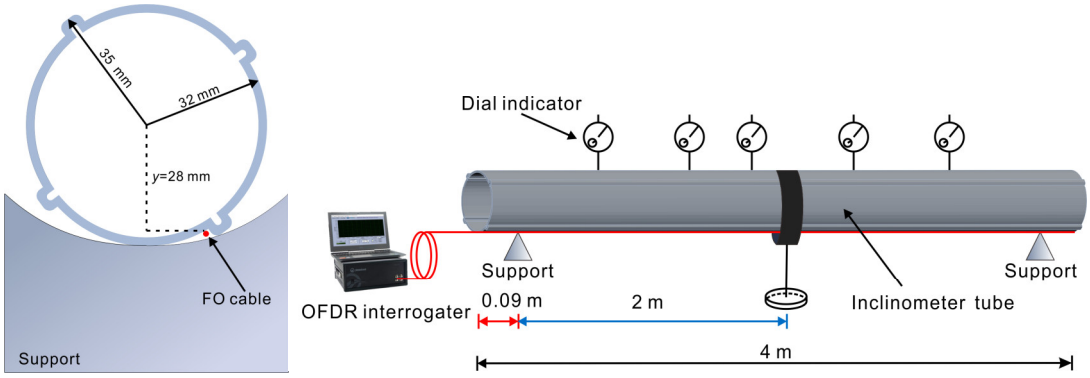

Fig. 7. Schematic of the three-point bending test of inclinometer tube.

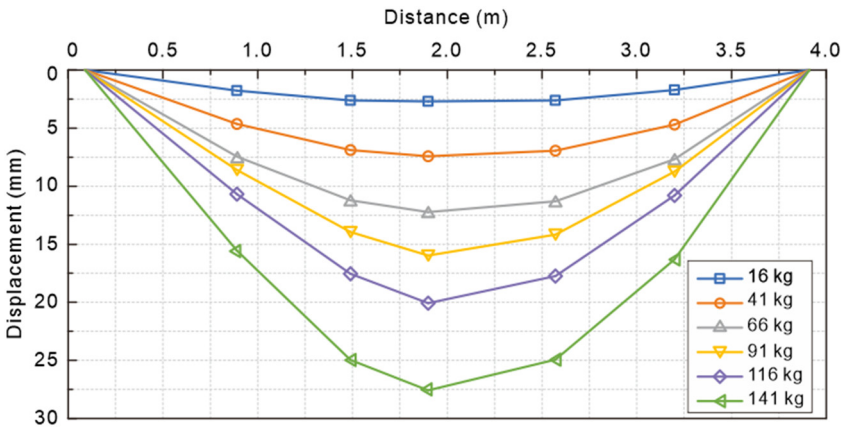

Fig. 8. Lateral displacement of inclinometer tube.

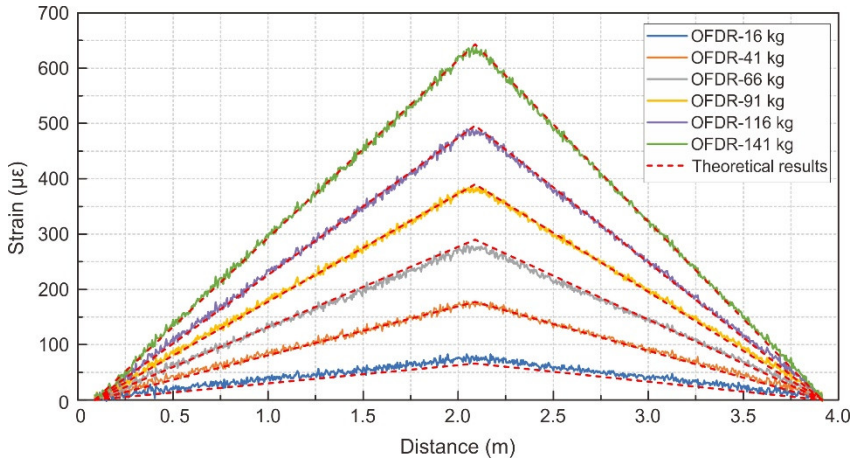

Fig. 9. Comparison of experimental (FO) and theoretical strains of inclinometer tube. The FO strains were corrected according to calculated strain transfer coefficients.

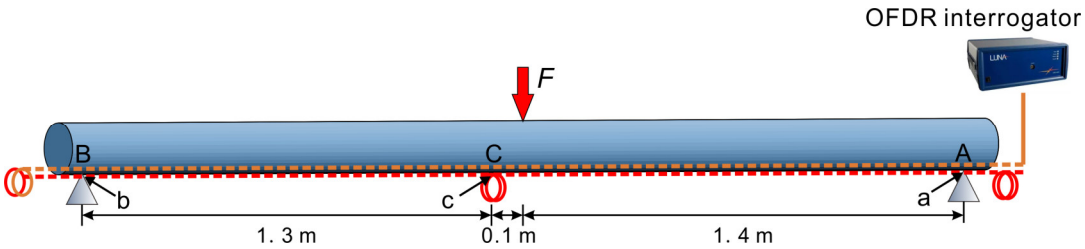

Fig. 10. Schematic of three-point bending test of PVC pipe.

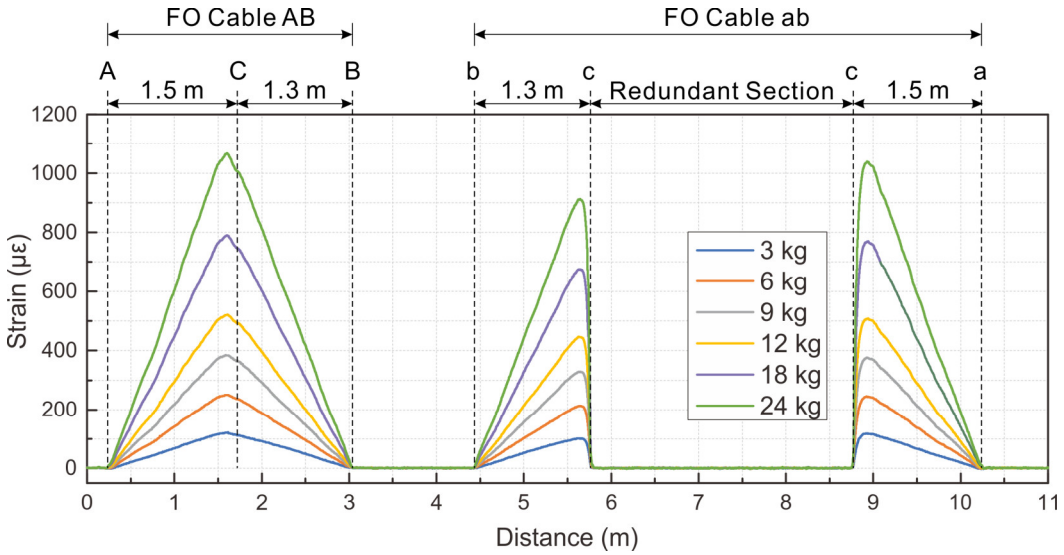

Fig. 11. Strain distributions of FO cables under each load.

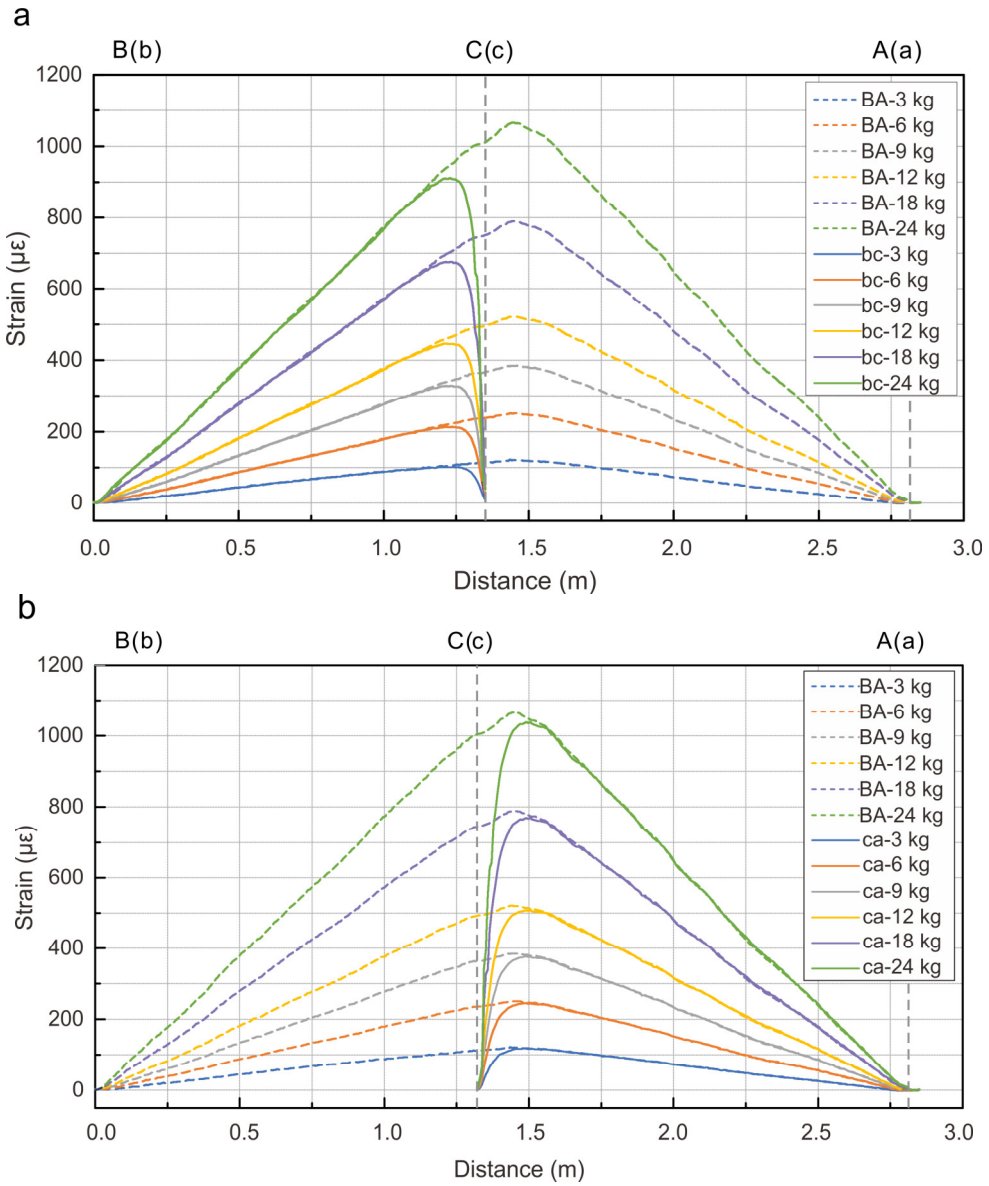

Fig. 12. Comparison of the strain distributions between cables AB and ab.

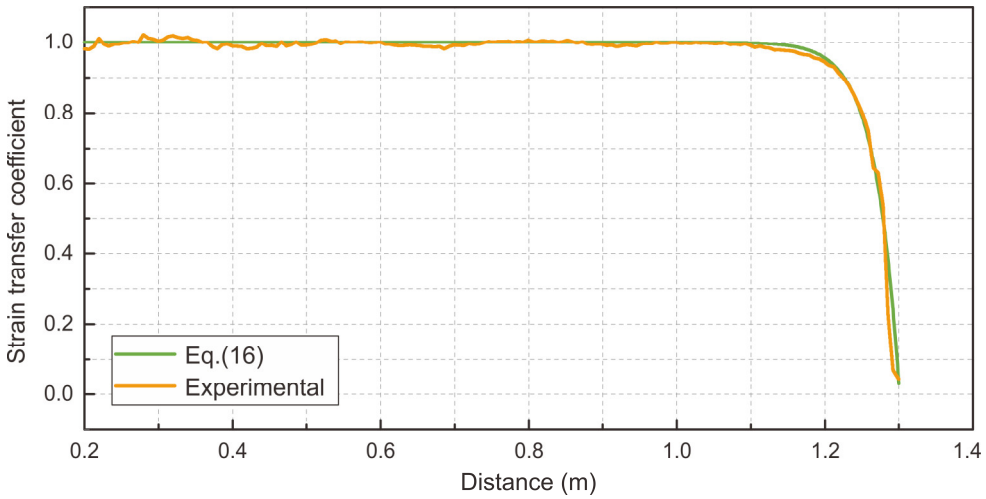

Fig. 13. Comparison between the experimental and theoretical strain transfer coefficients of cable bc.

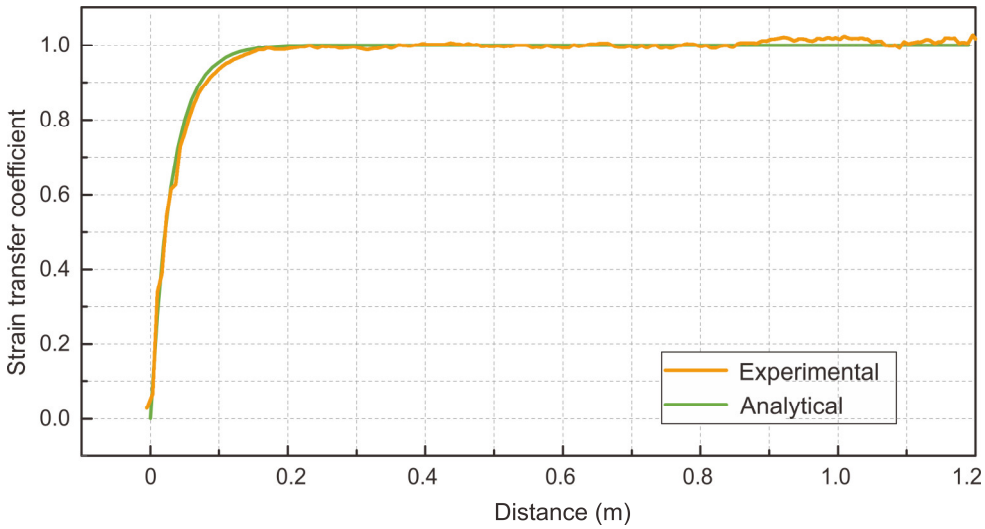

Fig. 14. Comparison between the experimental and theoretical strain transfer coefficients of cable ac.

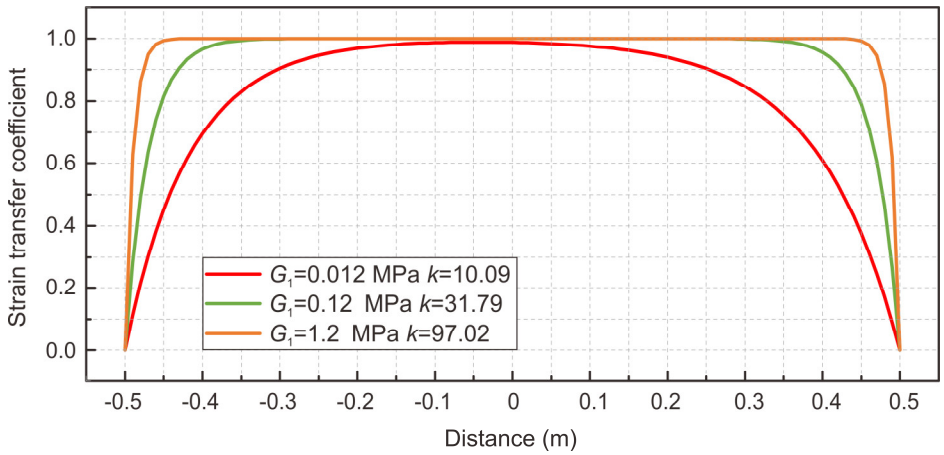

Fig. 15. Influence of shear modulus of inner coating on the strain transfer of FO sensor.

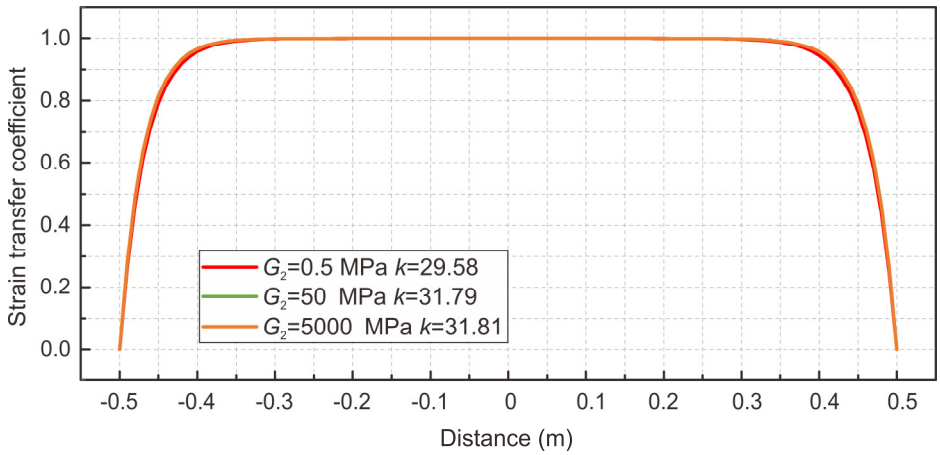

Fig. 16. Influence of shear modulus of outer coating on the strain transfer of FO sensor.

Table 1. Parameters of FO cable and adhesive layer used for strain transfer coefficient calculation (after ref. [16, 17, 30–33]).

Parameter	Symbol	Value	Unit
Radius of fiber core	r_c	62.5	μm
Young's modulus	E_c	72	GPa
Radius of inner coating	r_1	95	μm
Shear modulus of inner coating	G_1	0.12	MPa
Radius of outer coating	r_2	125	μm
Shear modulus of outer coating	G_2	50	MPa
Radius of jacket	r_3	900	μm
Shear modulus of outer coating	G_3	500	MPa
Minimum thickness of adhesive	t	200	μm
Shear modulus of adhesive layer	G_a	29	MPa